

Multi-Image Visual Question Answering for Unsupervised Anomaly Detection

Jun Li^{1,2}, Cosmin I. Bercea^{1,3}, Philip Müller¹, Lina Felsner¹, Suhwan Kim⁴, Daniel Rueckert^{1,2,5}, Benedikt Wiestler⁴, and Julia A. Schnabel^{1,2,3,6}

¹ Technical University of Munich, Germany

² Munich Center for Machine Learning, Germany

³ Helmholtz AI and Helmholtz Center Munich, Germany

⁴ Klinikum Rechts der Isar, Munich, Germany

⁵ Imperial College London, London, UK

⁶ King's College London, London, UK

Abstract. Unsupervised anomaly detection enables the identification of potential pathological areas by juxtaposing original images with their pseudo-healthy reconstructions generated by models trained exclusively on normal images. However, the clinical interpretation of resultant anomaly maps presents a challenge due to a lack of detailed, understandable explanations. Recent advancements in language models have shown the capability of mimicking human-like understanding and providing detailed descriptions. This raises an interesting question: *How can language models be employed to make the anomaly maps more explainable?* To the best of our knowledge, we are the first to leverage a language model for unsupervised anomaly detection, for which we construct a dataset with different questions and answers. Additionally, we present a novel multi-image visual question answering framework tailored for anomaly detection, incorporating diverse feature fusion strategies to enhance visual knowledge extraction. Our experiments reveal that the framework, augmented by our new Knowledge Q-Former module, adeptly answers questions on the anomaly detection dataset. Besides, integrating anomaly maps as inputs distinctly aids in improving the detection of unseen pathologies. Code available at: <https://lijunrio.github.io/Multi-Image-VQA-for-UAD/>.

Keywords: Multi-Modalities · Multi-Image Fusion · Language Models

1 Introduction

Unsupervised Anomaly Detection (UAD) plays a vital role in early disease diagnosis. Most UAD methods follow a reconstruction-based manner [2, 31], which utilizes Auto-Encoders (AEs) [3] to solely train on normal data, thereby learning the distribution of the healthy data. When faced with non-healthy data, considered as out-of-distribution images, AEs still attempt to reconstruct them within a healthy distribution, resulting in a pseudo-healthy (PH) reconstruction. Anomaly maps highlight potential abnormal areas within the image by comparing the original input and its reconstruction. These maps and reconstructions

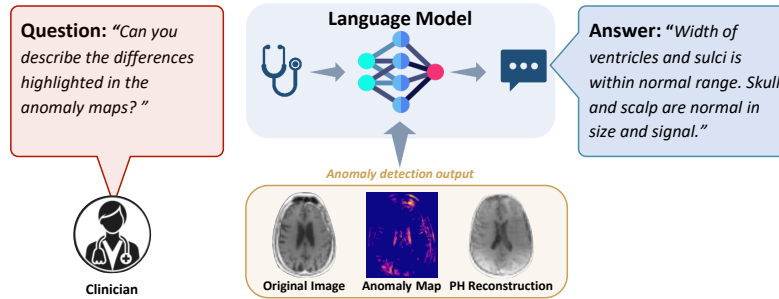


Fig. 1. Our framework is designed to process questions in conjunction with results from anomaly detection methods aiming to provide clinicians with clear, interpretable responses that render anomaly map analyses more intuitive and clinically actionable.

can guide clinicians in their diagnosis, offering valuable insights for more precise clinical assessment. Yet, due to the inherent nature of unsupervised learning, the direct interpretability of UAD findings is limited, with clinicians lacking explicit explanations of the detected anomalies. Thus, there is a clear imperative to augment the clarity and user-friendliness of UAD outputs to better support clinical decision-making.

In recent years, language models [4, 20, 25] have reached human-like performance in question answering, summarizing, reasoning, and knowledge retrieval. Moreover, in some medical tasks, these models even pass the medical licensing examination in the United States [9]. The outstanding performance of language models gives rise to an interesting idea: combining a language model and UAD may potentially provide better, comprehensive explanatory text descriptions for clinicians. However, it is worth noting that the majority of existing language models are trained for a single modality. Therefore, when adapted to multi-modal tasks, such as Visual Question Answering (VQA), large amounts of data are usually required for fine-tuning [14, 30]. In the medical field, the availability of vast annotated data is challenging, which means that exploring methods to enhance the performance of language models on small datasets is an important research direction [13, 19]. Moreover, when incorporating a language model into UAD, the task transforms from a straightforward single-image problem to a more complicated multi-image VQA challenge. While numerous works have been proposed for medical VQA [1, 16, 26], they mainly focus on a single image as input. Recently, some studies [12, 24, 29] have begun focusing on generating radiology reports from frontal and lateral views of X-rays, similar to answering questions based on multiple given images. Nevertheless, there is a notable absence of a benchmark for simultaneously processing three images for the VQA task.

To address these gaps, we developed, to the best of our knowledge, the first multi-image question answering benchmark based on unsupervised anomaly detection. Our framework designs different feature fusion strategies for combining the anomaly map, original image, and PH reconstruction. Besides, inspired by the Querying Transformer (Q-Former) [13], we propose a Knowledge Q-Former (KQ-

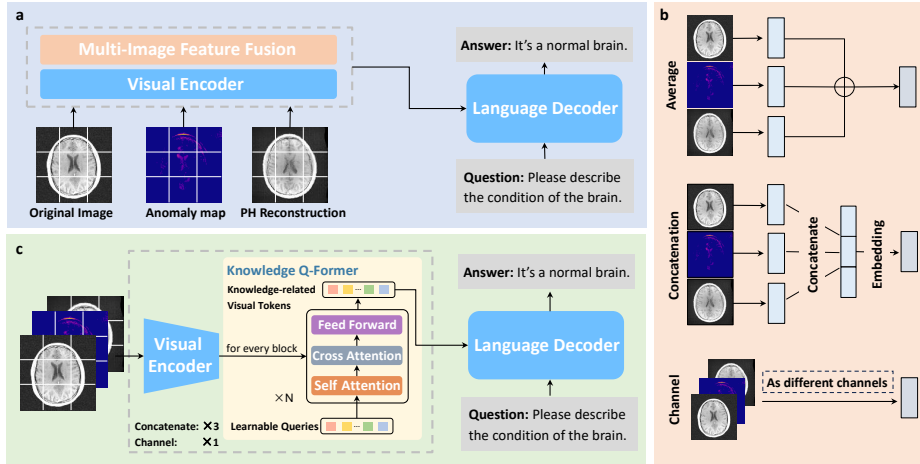


Fig. 2. An overview of our proposed frameworks. (a) the multi-image VQA framework; (b) multi-image feature fusion strategies; (c) knowledge Q-former framework.

Former) module to assist the framework in extracting visual features related to textual knowledge. Extensive experiments have been conducted to verify the effectiveness of the framework and proposed KQ-Former module. Additionally, we explore the influence of the anomaly map for the framework in facing unknown anomalies. Overall, our main contributions can be summarized as follows:

- We construct a multi-image VQA dataset for unsupervised anomaly detection, annotated by medical experts and covering various conditions.
- We propose a model-agnostic VQA framework with different image feature fusion strategies and a KQ-Former module to enhance the model in extracting knowledge-related visual features.
- We demonstrate improved performance of our KQ-Former module on VQA tasks, and show that anomaly maps improve unseen pathology detection.

2 Methods

2.1 Problem Statement

For the i -th image triple (I_i^o, I_i^a, I_i^r) in the dataset \mathcal{D} , consisting of the original medical image I_i^o , anomaly map I_i^a , and PH reconstruction I_i^r , alongside the corresponding question Q_i , the goal of our framework is to generate the answer A_i related to the images and question. Figure 3 provides an overview of our two frameworks: the multi-image VQA framework with different fusion strategies, as well as the proposed Knowledge Q-former framework.

2.2 Multi-Image VQA Framework

Most existing VQA methods [16, 19] only focus on a single image, lacking a baseline for UAD to handle three images simultaneously. Therefore, we design a multi-image VQA framework as the baseline method. Inspired by the report generation [12, 29], which usually fuses the frontal and lateral views of X-rays via average aggregation and concatenation, we also utilize these two methods to fuse the visual features. Besides, considering the anomaly map and PH reconstruction as variations of the original image, we also design a channel-wise fusion strategy.

Visual Encoder. Given image triple $\mathcal{I} = (I_i^o, I_i^a, I_i^r)$, $I_i \in \mathbb{R}^{H \times W \times C}$ as input, with H, W, C are height, width, and channel respectively. The shared-weight visual encoder extracts visual embedding by $\mathcal{V} = \mathcal{F}_v(\mathcal{I})$, for each embedding triple $\mathcal{V} = (V_i^o, V_i^a, V_i^r)$, $V_i \in \mathbb{R}^{n \times d}$, where n represents the number of patches and d denotes the embedding dimension in the image.

Figure 3 (b) illustrates the three fusion strategies in the framework. The first method is fusing the image features through an average aggregation expressed as $V_i' = \frac{1}{3} \sum_{j \in \{o, a, r\}} V_i^j$. The second method combines visual features through concatenation, denoted as $C_i = [V_i^o; V_i^a; V_i^r]$, $C_i \in \mathbb{R}^{3n \times d}$. Subsequently, a trainable projection model $\Phi(\cdot)$ is employed to reduce the dimension of C_i into $V_i' = \Phi(C_i)$, where $\Phi(\cdot)$ consists of a two-layer multilayer perceptron. For the last strategy, we convert each image to a single-channel image $I_i \in \mathbb{R}^{H \times W \times 1}$, and use them as different channels of a combined image $\hat{I}_i = [I_i^o, I_i^a, I_i^r] \in \mathbb{R}^{H \times W \times 3}$. Therefore, the multi-image VQA problem has been transferred into a single image VQA. The final merged visual features can be expressed as $V_i' = \mathcal{F}_v(\hat{I}_i)$.

Language Decoder. Unlike many existing methods [16, 19] that simplify VQA as the classification task, our framework treats it as a natural language generation task [12, 24, 29]. The language decoder takes a question Q_i and the merged image features V_i' as input to generate the answer A_i token by token. At each time step t , the decoder produces a probability distribution of each token $p_\theta(A_i^t)$ over vocabulary. Thus, the distribution of answer A_i with length T is given as: $p_\theta(A_i) = \prod_{t=1}^T p_\theta(A_i^t | Q_i, V_i', A_i^1, A_i^2, \dots, A_i^{t-1})$.

During the training process, the framework aims to minimize the negative log-likelihood, where N is the number of training samples. Therefore, the language modeling loss can be defined as:

$$\mathcal{L}(\theta^*) = \arg \min_{\theta} \sum_{i=1}^N -\log p_\theta(A_i | Q_i, V_i') \quad (1)$$

2.3 Knowledge Q-Former Framework

Aligning visual and textual features in language models is often prohibitively expensive and data-intensive. To enhance performance on small datasets, we propose a Knowledge Q-Former (KQ-Former), which is shown in Figure 3 (c). In

Anomaly Category			Closed Questions:
posttreatment change 26%	lesions 13%	enlarged ventricles 11%	1) Is the case normal? Yes./No. (2) 2) Please describe the condition of the brain. It's + category. (8 anomalies + 1 normal brain)
	edema 11%	craniotomy 9%	3) Can you comment on the severity of the pathology? Clinically irrelevant. / Potentially clinically relevant. / Clinically relevant. / Not applicable. (4)
mass lesion 15%	artefacts 9%	resection 6%	Open Questions:
			1a) Are there areas in the anomaly maps that highlight a normal variation of the healthy, rather than pathological areas (false positives)? 1b) Can you describe the differences highlighted between anomaly maps and origin image and why it is the healthy region? 2) Is the pseudo-healthy reconstruction a plausible restoration of the input to a healthy state? 3) Do the anomaly maps accurately reflect the selected disease?

Fig. 3. Overview of the anomaly dataset. Left: category distribution of anomalies. Right: definition of closed and open questions. For closed questions: blue text shows the answer type, number in parentheses denotes the count of answer types.

contrast to [13], which includes two transformer submodules [27] for image and text, we streamline it into a single transformer. This adjustment is motivated by the constraints in the medical field, where datasets typically contain only a few hundred samples, significantly smaller than those in general fields. The symmetric structure and multi-tasking in the original Q-Former would substantially increase complexity and introduce redundancy. Additionally, we initialize the KQ-Former module with BioBERT [10]. This facilitates knowledge transfer, enabling the model to learn knowledge-related visual features during training.

Specifically, the input of our KQ-Former is learnable queries $L_i \in \mathbb{R}^{32 \times 768}$, and the image feature V_i is fed into the cross-attention layer. This enables L_i to interact with the visual feature V_i during the training, and KQ-Former gradually merges the visual features with the knowledge embedded in the pre-trained weights. Consequently, the output visual token $K_i \in \mathbb{R}^{32 \times 768}$ not only contains key information from the image but is also more related to textual knowledge. Subsequently, we utilize K_i as the input for the language decoder.

Figure 3 (c) illustrates two methods to combine the output visual token K_i . The first one is concatenating the token from different images to get $K'_i = [K_i^o; K_i^a; K_i^r]$, $K'_i \in \mathbb{R}^{96 \times 768}$ and utilizing it as the input of the language decoder. The second method is to initially combine the three images channel-wise and obtain $\hat{I}_i = [I_i^o, I_i^a, I_i^r] \in \mathbb{R}^{H \times W \times 3}$. We then utilized $\mathcal{F}(\hat{I}_i)$ as the input of the cross-attention layer in KQ-Former. Thus, the output visual token can be directly employed as the input of the language model, which includes the information of different images. Finally, the language modeling remains consistent with Sec.2.2.

3 Experiments

Dataset. We collected 440 T1 weighted MRI 2D mid-axial brain images from the fastMRI dataset [8], containing healthy (N=253) and unhealthy (N=187) data. The dataset features 8 distinct types of anomalies for the primary experiment and an additional 17 cases across 6 different pathologies to assess

Table 1. Comparison results. The KQF framework considerably outperforms the MI framework, with ViT as the backbone superior to ResNet50. Concatenation and channel strategies typically exceed average aggregation. B1 to B4 denote BLEU-1 to BLEU-4, while RL and Cr denote ROUGE-L and CIDEr. Best two performances are in **bold**.

Backbone	Method	Closed		Open					
		ACC \uparrow	F1 \uparrow	B1 \uparrow	B2 \uparrow	B3 \uparrow	B4 \uparrow	RL \uparrow	Cr \uparrow
ResNet	MI _{average}	36.49	38.89	0.44	0.35	0.29	0.24	0.57	1.82
	MI _{concat}	40.54	43.89	0.35	0.26	0.21	0.18	0.56	1.48
	MI _{channel}	36.49	38.89	0.38	0.29	0.24	0.20	0.54	1.69
	KQF _{concat}	54.05	47.27	0.47	0.37	0.30	0.25	0.60	1.97
	KQF _{channel}	47.97	41.54	0.45	0.36	0.31	0.27	0.58	1.90
ViT	MI _{average}	56.76	49.30	0.49	0.38	0.32	0.27	0.62	1.94
	MI _{concat}	57.43	50.14	0.45	0.35	0.29	0.24	0.61	1.79
	MI _{channel}	53.38	48.33	0.44	0.34	0.28	0.24	0.58	1.77
	KQF _{concat}	60.14	56.92	0.55	0.48	0.44	0.41	0.67	2.84
	KQF _{channel}	60.81	55.93	0.51	0.43	0.38	0.34	0.65	2.50

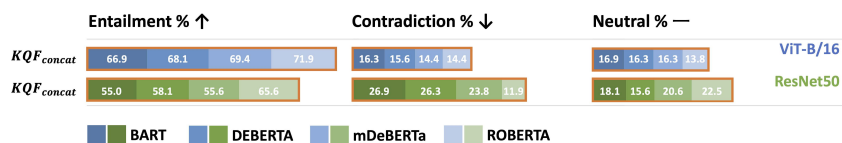


Fig. 4. Evaluation results on open questions by different NLI models.

the model’s generalization capabilities to unseen pathological conditions. The anomaly maps and PH reconstructions were generated by a generative network in [2]. Two senior neuroradiologists annotated the questions, including both closed and open types, as defined in Figure 3. Subsequently, the data was structured into question-answer pairs and divided into training, validation, and test sets in a 7:1:2 ratio, with 1078, 308, and 154 samples, respectively. Particularly, each disease and question type were included in every set without any overlap.

Implementation. Our framework is model-agnostic. We selected ViT-B/16 [5] and ResNet50 [6] as the backbones of the visual encoder. For the language decoder, we chose GPT-2 small [22]. Both the multi-image VQA and KQ-Former frameworks were trained on a single NVIDIA RTX A6000 for 40 epochs, using early stopping with a patience of 10. We utilized the AdamW optimizer [18], a learning rate of $1.5e-5$ and a weight decay of 0.05. During generation, we used beam search with a width of 5. For evaluation, we employed Accuracy (ACC) and F1 score for closed questions, and two types of metrics for open questions without a fixed answer format. The first includes BLEU scores [21], ROUGE-L [15], and CIDEr [28] for comparing the similarity between ground truth and predicted sentences. The second involves utilizing Natural Language Inference (NLI) models [7, 11, 17, 23] to evaluate the entailment between sentences.

Performance Comparison. Table 1 and Figure 4 show the performance of our Multi-Image VQA (MI) and KQ-Former (KQF) frameworks. We can observe that

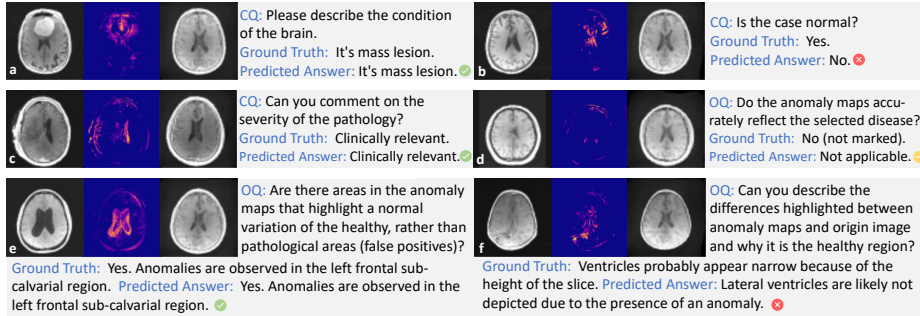


Fig. 5. Positive (a,c,e) and negative(b,d,f) examples of the KQ-Former framework with concatenation strategy. Each example includes an original image, anomaly map and PH reconstructions from left to right. CQ and OQ represent closed and open questions.

with the ViT backbone, both the MI and KQF frameworks generally achieve better results compared to ResNet50. Besides, the KQF framework considerably outperforms the MI frameworks. For example, when utilizing the ResNet50 backbone with the concatenation strategy, the accuracy for closed questions rises from 40.54% to 54.05%, and the BLEU-4 score for open questions increased by 38.89% compared to the MI framework. The KQF with the ViT backbone shows the overall best performance, with similar outcomes for both fusion strategies. Results remain similar when evaluated by NLI models, KQF with concatenation and channel strategy show a higher mean entailment ratio of 69.1% and 67.0%, with a lower mean contradiction ratio of 15.2% and 17.3% compared to others as shown in Figure 4. Details and visualization examples of each NLI model can be found in the supplementary material. Figure 5 shows some results of KQF with concatenation strategy. The model can understand the questions and provide corresponding answers for all examples, despite occasional errors.

Benefits of Anomaly Maps. In this section, we compare whether adding anomaly maps (A) and PH reconstructions (R) can improve performance on closed questions. We select the KQF frameworks with ViT (best in Table 1) as the backbone to retrain the framework. For framework consistency, we utilize “black” images (B) to mask missing inputs. Table 2 shows that the combination of original, anomaly, and black images (O-A-B) generally performs the best, especially in Q1. Additionally, with the channel strategy, there is a 25.28% improvement in F1 for Q3 compared to O-B-B, whereas using both an anomaly map and PH reconstruction (O-A-R) led to a 9.23% decrease compared to O-A-B. We also note that for the concatenation strategy, the model performs exceptionally with only the anomaly map for Q3. These results suggest that anomaly maps can help the framework focus on the essential information of the image and enhance performance, whereas PH reconstruction introduces ambiguity in the training as it represents a pseudo-healthy format of the original image. However, we believe that for open questions (including image comparisons), it is necessary and ben-

eficial to include the PH reconstruction as input.

Table 2. Benefits of anomaly maps for closed questions. O, A, R, and B represent the original image, anomaly map, PH reconstruction, and black image, respectively.

Method	Image	Q1		Q2		Q3	
		ACC \uparrow	F1 \uparrow	ACC \uparrow	F1 \uparrow	ACC \uparrow	F1 \uparrow
KQF _{concat}	O-B-B	85.29	85.29	37.50	33.02	42.50	33.85
	O-A-B	88.24	88.19	32.50	30.35	52.50	42.16
	O-A-R	86.76	86.76	27.50	21.83	42.50	40.35
	B-A-B	79.41	79.34	32.50	24.89	52.50	51.07
	O-B-R	79.41	78.75	30.00	23.20	45.00	45.80
KQF _{channel}	O-B-B	89.71	89.69	27.50	18.80	52.50	45.56
	O-A-B	91.18	91.15	30.00	18.59	60.00	57.08
	O-A-R	85.29	85.28	22.50	8.27	52.50	51.81
	B-A-B	88.24	88.24	25.00	20.10	42.50	42.64
	O-B-R	82.35	82.29	27.50	20.33	42.50	38.08

Table 3. Experiments for unseen anomalies on an additional dataset for CQ 1.

Method	Image	Overall		Unhealthy (17%)		Healthy (83%)	
		ACC \uparrow	F1 \uparrow	ACC \uparrow	F1 \uparrow	ACC \uparrow	F1 \uparrow
KQF _{concat}	O-B-B	84.13	87.50	69.57	80.00	98.70	95.00
	O-A-B	89.37	89.37	82.35	82.35	96.39	96.39
	O-A-R	81.74	83.06	68.42	72.22	95.06	93.90
	B-A-B	81.31	84.38	65.22	75.00	97.40	93.75
	O-B-R	84.52	83.67	75.00	72.73	94.05	94.61
KQF _{channel}	O-B-B	84.45	87.00	71.43	78.95	97.47	95.06
	O-A-B	85.72	88.85	72.73	82.05	98.72	95.65
	O-A-R	82.81	85.67	68.18	76.92	97.44	94.41
	B-A-B	84.13	87.50	69.57	80.00	98.70	95.00
	O-B-R	84.45	87.00	71.43	78.95	97.47	95.06

Performance on Unseen Anomalies. In this section, we employ the model from Table 2 to assess whether anomaly maps can aid the framework in detecting unknown anomalies. To simulate a real clinical environment, this unseen dataset contains a large amount of healthy data (83%) and a small amount of anomalies (17%), where the 6 unknown conditions were never shown in the training set (for the category distribution see supplementary material). Table 3 shows that the inclusion of the anomaly map (O-A-B) significantly increases overall accuracy. For example, in the KQ-Former model with concatenation strategy, the accuracy increased from 84.13% to 89.37% compared to O-B-B, and there is a considerable 18.37% improvement of the accuracy in identifying unhealthy data. Similarly, adding both the anomaly map and PH reconstruction (O-A-R) leads to a decline, possibly also due to the ambiguity mentioned in the previous section.

4 Conclusion

In this work, we integrated language models for UAD and designed, to the best of our knowledge, the first multi-image VQA benchmarks for anomaly detection. Additionally, we proposed a KQ-Former module to enhance the framework’s ability to extract knowledge-related visual features on a small dataset. Experimental results showed a considerable improvement for our KQ-Former frameworks, which means that the proposed KQ-Former module can successfully assist the framework in extracting knowledge-related visual features that are more suitable for the VQA task. Besides, the results on unseen anomalies also suggest that anomaly maps can help the framework focus on essential information and improve the performance on unseen pathologies.

Our findings highlight the potential for enhancing the explanation of anomaly detection by harnessing language models, empowering further advancements in clinical diagnosis.

References

1. Bai, L., Islam, M., Ren, H.: Cat-vil: Co-attention gated vision-language embedding for visual question localized-answering in robotic surgery. In: *Medical Image Computing and Computer-Assisted Intervention*. pp. 397–407. Springer (2023)
2. Bercea, C.I., Wiestler, B., Rueckert, D., Schnabel, J.A.: Generalizing unsupervised anomaly detection: Towards unbiased pathology screening. In: *Medical Imaging with Deep Learning* (2023)
3. Bourlard, H., Kamp, Y.: Auto-association by multilayer perceptrons and singular value decomposition. *Biological cybernetics* **59**(4-5), 291–294 (1988)
4. Chowdhery, A., Narang, S., Devlin, J., Bosma, M., Mishra, G., Roberts, A., Barham, P., Chung, H.W., Sutton, C., et al.: Palm: Scaling language modeling with pathways. *Journal of Machine Learning Research* **24**(240), 1–113 (2023)
5. Dosovitskiy, A., Beyer, L., Kolesnikov, A., Weissenborn, D., Zhai, X., Unterthiner, T., Dehghani, M., Minderer, M., Heigold, G., Gelly, S., Uszkoreit, J., Houlsby, N.: An image is worth 16x16 words: Transformers for image recognition at scale. In: *International Conference on Learning Representations* (2021)
6. He, K., Zhang, X., Ren, S., Sun, J.: Deep residual learning for image recognition. In: *Proceedings of the IEEE Conference on Computer Vision and Pattern Recognition*. pp. 770–778 (2016)
7. He, P., Gao, J., Chen, W.: Debertav3: Improving deberta using electra-style pre-training with gradient-disentangled embedding sharing. In: *The Eleventh International Conference on Learning Representations* (2022)
8. Knoll, F., Zbontar, J., Sriram, A., Muckley, M.J., Bruno, M., Defazio, A., Parente, M., Geras, K.J., Katsnelson, J., et al.: fastmri: A publicly available raw k-space and dicom dataset of knee images for accelerated mr image reconstruction using machine learning. *Radiology: Artificial Intelligence* **2**(1), e190007 (2020)
9. Kung, T.H., Cheatham, M., Medenilla, A., Sillos, C., De Leon, L., Elepaño, C., et al.: Performance of chatgpt on usmle: Potential for ai-assisted medical education using large language models. *PLoS digital health* **2**(2), e0000198 (2023)
10. Lee, J., Yoon, W., Kim, S., Kim, D., Kim, S., So, C.H., Kang, J.: Biobert: a pre-trained biomedical language representation model for biomedical text mining. *Bioinformatics* **36**(4), 1234–1240 (2020)

11. Lewis, M., Liu, Y., Goyal, N., et al.: BART: Denoising sequence-to-sequence pre-training for natural language generation, translation, and comprehension. In: Proceedings of the Association for Computational Linguistics. pp. 7871–7880 (2020)
12. Li, J., Li, S., Hu, Y., Tao, H.: A self-guided framework for radiology report generation. In: Medical Image Computing and Computer-Assisted Intervention. pp. 588–598. Springer (2022)
13. Li, J., Li, D., Xiong, C., Hoi, S.: Blip: Bootstrapping language-image pre-training for unified vision-language understanding and generation. In: International Conference on Machine Learning. pp. 12888–12900. PMLR (2022)
14. Li, P., Liu, G., He, J., Zhao, Z., Zhong, S.: Masked vision and language pre-training with unimodal and multimodal contrastive losses for medical visual question answering. In: Medical Image Computing and Computer-Assisted Intervention. pp. 374–383. Springer (2023)
15. Lin, C.Y.: Rouge: A package for automatic evaluation of summaries. In: Text summarization branches out. pp. 74–81 (2004)
16. Liu, B., Zhan, L.M., Wu, X.M.: Contrastive pre-training and representation distillation for medical visual question answering based on radiology images. In: Medical Image Computing and Computer Assisted Intervention. pp. 210–220. Springer (2021)
17. Liu, Y., Ott, M., Goyal, N., Du, J., et al.: Roberta: A robustly optimized bert pretraining approach. arXiv preprint arXiv:1907.11692 (2019)
18. Loshchilov, I., Hutter, F.: Decoupled weight decay regularization. In: International Conference on Learning Representations (2018)
19. Nguyen, B.D., Do, T.T., Nguyen, B.X., Do, T., Tjiputra, E., Tran, Q.D.: Overcoming data limitation in medical visual question answering. In: Medical Image Computing and Computer Assisted Intervention. pp. 522–530. Springer (2019)
20. OpenAI: Introducing ChatGPT (2023), <https://openai.com/blog/chatgpt/>, November 30, 2022
21. Papineni, K., Roukos, S., Ward, T., Zhu, W.J.: Bleu: a method for automatic evaluation of machine translation. In: Proceedings of the 40th annual meeting of the Association for Computational Linguistics. pp. 311–318 (2002)
22. Radford, A., Wu, J., Child, R., Luan, D., Amodei, D., Sutskever, I., et al.: Language models are unsupervised multitask learners. OpenAI blog **1**(8), 9 (2019)
23. Sileo, D.: Tasksource: Structured dataset preprocessing annotations for frictionless extreme multi-task learning and evaluation. arXiv preprint arXiv:2301.05948 (2023)
24. Tanida, T., Müller, P., Kaissis, G., Rueckert, D.: Interactive and explainable region-guided radiology report generation. In: Proceedings of the IEEE Conference on Computer Vision and Pattern Recognition. pp. 7433–7442 (June 2023)
25. Touvron, H., Lavril, T., Izacard, G., Martinet, X., Lachaux, M.A., Lacroix, T., Rozière, B., Goyal, N., Hambro, E., et al.: Llama: Open and efficient foundation language models. arXiv preprint arXiv:2302.13971 (2023)
26. Van Sonsbeek, T., Derakhshani, M.M., Najdenkoska, I., Snoek, C.G., Worring, M.: Open-ended medical visual question answering through prefix tuning of language models. In: Medical Image Computing and Computer Assisted Intervention. pp. 726–736. Springer (2023)
27. Vaswani, A., Shazeer, N., Parmar, N., Uszkoreit, J., Jones, L., Gomez, A.N., Kaiser, Ł., Polosukhin, I.: Attention is all you need. In: Advances in Neural Information Processing Systems. vol. 30 (2017)

28. Vedantam, R., Lawrence Zitnick, C., Parikh, D.: Cider: Consensus-based image description evaluation. In: Proceedings of the IEEE Conference on Computer Vision and Pattern Recognition. pp. 4566–4575 (2015)
29. Wu, X., Yang, S., Qiu, Z., Ge, S., Yan, Y., Wu, X., Zheng, Y., Zhou, S.K., Xiao, L.: Deltanet: Conditional medical report generation for covid-19 diagnosis. In: Proceedings of the 29th International Conference on Computational Linguistics. pp. 2952–2961 (2022)
30. Zhang, X., Wu, C., Zhao, Z., Lin, W.o.: Pmc-vqa: Visual instruction tuning for medical visual question answering. arXiv preprint arXiv:2305.10415 (2023)
31. Zimmerer, D., Isensee, F., Petersen, J., Kohl, S., Maier-Hein, K.: Unsupervised anomaly localization using variational auto-encoders. In: Medical Image Computing and Computer Assisted Intervention. pp. 289–297. Springer (2019)

Supplementary Material for Multi-Image Visual Question Answering for Unsupervised Anomaly Detection

Jun Li^{1,2}, Cosmin I. Bercea^{1,3}, Philip Müller¹, Lina Felsner¹, Suhwan Kim⁴, Daniel Rueckert^{1,2,5}, Benedikt Wiestler⁴, and Julia A. Schnabel^{1,2,3,6}

- ¹ Technical University of Munich, Germany
² Munich Center for Machine Learning, Germany
³ Helmholtz AI and Helmholtz Center Munich, Germany
⁴ Klinikum Rechts der Isar, Munich, Germany
⁵ Imperial College London, London, UK
⁶ King's College London, London, UK

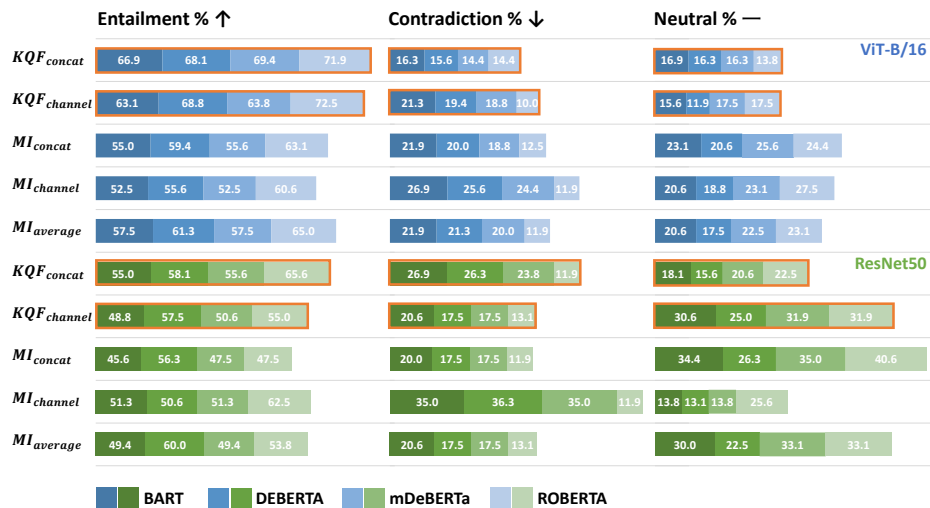


Fig. 1. Evaluation results on open questions by different Nature Language Inference (NLI) models. The NLI model categorizes whether the given hypothesis (predicted sentence) and the premise (ground truth) logically imply (entailment), oppose (contradiction), or are indeterminate (neutral) to each other. We can observe that the KQF frameworks have the highest entailment ratio across different NLI models in most cases. Additionally, the contradiction ratios are lower compared to the MI frameworks, consistent with Table 1 results (main paper). Also, utilizing ViT yields better results than using ResNet as the backbone. References for the four NLI models see the main paper.

<p>Framework: KQF-channel-ViT</p> <p>Question: Can you describe the differences highlighted between anomaly maps and origin image and why it is the healthy region?</p> <p>Ground Truth: Width of left lateral ventricle is within normal range.</p> <p>Predict Answer: Sulci are unremarkable in size.</p>	<ul style="list-style-type: none"> ■ BART: Neutral ■ DEBERTA: Neutral ■ mDeBERTa: Entailment ■ ROBERTA: Entailment
<p>Framework: KQF-channel-ResNet</p> <p>Question: Are there areas in the anomaly maps that highlight a normal variation of the healthy, rather than pathological areas (false positives)?</p> <p>Ground Truth: Yes. Anomalies are observed in the left frontal and right occipital sulci.</p> <p>Predict Answer: Yes. There are anomalies observed in parts of the lateral ventricles and some of the sulci.</p>	<ul style="list-style-type: none"> ■ BART: Neutral ■ DEBERTA: Neutral ■ mDeBERTa: Neutral ■ ROBERTA: Entailment
<p>Framework: KQF-channel-ViT</p> <p>Question: Can you describe the differences highlighted between anomaly maps and origin image and why it is the healthy region?</p> <p>Ground Truth: Width of sulci is within normal range.</p> <p>Predict Answer: Not applicable.</p>	<ul style="list-style-type: none"> ■ BART: Contradiction ■ DEBERTA: Contradiction ■ mDeBERTa: Contradiction ■ ROBERTA: Entailment
<p>Framework: KQF-concate-ViT</p> <p>Question: Is the pseudo-healthy reconstruction a plausible restoration of the input to a healthy state?</p> <p>Ground Truth: No (there is an unnatural shape in the left lateral horn).</p> <p>Predict Answer: No (there is an unnatural shape in the left lateral horn).</p>	<ul style="list-style-type: none"> ■ BART: Entailment ■ DEBERTA: Entailment ■ mDeBERTa: Entailment ■ ROBERTA: Entailment
<p>Framework: KQF-concate-ViT</p> <p>Question: Do the anomaly maps accurately reflect the selected disease?</p> <p>Ground Truth: Yes (however, only partial marking of anomaly).</p> <p>Predict Answer: Yes.</p>	<ul style="list-style-type: none"> ■ BART: Entailment ■ DEBERTA: Entailment ■ mDeBERTa: Entailment ■ ROBERTA: Entailment
<p>Framework: KQF-concate-ViT</p> <p>Question: Are there areas in the anomaly maps that highlight a normal variation of the healthy, rather than pathological areas (false positives)?</p> <p>Ground Truth: Yes. There are anomalies in the left frontal sulci.</p> <p>Predict Answer: No.</p>	<ul style="list-style-type: none"> ■ BART: Contradiction ■ DEBERTA: Contradiction ■ mDeBERTa: Contradiction ■ ROBERTA: Contradiction

Fig. 2. Positive and negative samples from different NLI models. In certain instances, different models may have different judgments, indicating that the results may still exhibit some deviations from human recognition. For example, in the first case, the KQF framework predicts “Sulci are unremarkable in size” and the ground truth is “Width of left lateral ventricle is within normal range”. The BART and DEBERTA models classify as “Neutral”, while mDeBERTa and ROBERTA predict as “Entailment”.

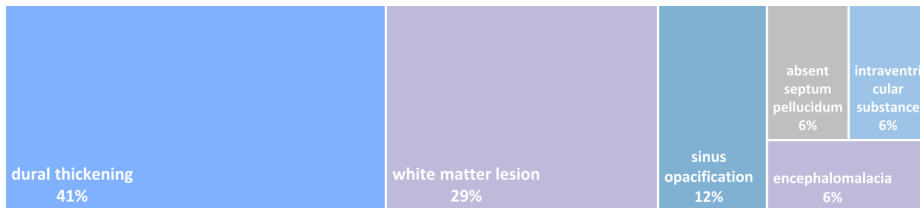


Fig. 3. Category distribution of unseen anomalies. These unseen anomalies are dural thickening, white matter lesion, sinus opacification, encephalomalacia, intraventricular substance, and absent septum pellucidum.